RSC Advances

PAPER

View Article Online
View Journal | View Issue

Cite this: *RSC Adv.*, 2025, **15**, 39431

Uric acid electrochemical biosensor based on a laser-induced graphene electrode modified with a Honey-mediated nanocomposite of reduced graphene oxide and bimetallic silver–cobalt

Isa Anshori, †*[ab] Arini Rahma Adzkia,†[a] Uperianti,[ac] Suksmandhira Harimurti, *[dj] Nurrahmi Handayani,[be] Veinardi Suendo, [bf] Muhammad Ali Zulfikar,[e] Annop Klamchuen, [g] Chih-Yu Chang[h] and Murni Handayani*[i]

Abnormal uric acid (UA) levels are commonly linked to several metabolomic or internal organ problems. Electrochemical-based tests have been used as alternative early screening methods to determine the levels of biomarkers, including UA. Electrochemical biosensors based on laser-induced graphene (LIG) electrodes could offer a promising alternative to realize a low-cost biosensor for biomarker detection. In this study, an LIG electrode was modified with a nanocomposite composed of reduced graphene oxide and silver–cobalt bimetal (rGO/AgCo), resulting in its enhanced sensitivity and selectivity for the detection of UA. Furthermore, to promote eco-friendliness, honey was utilized as the mediator to reduce and stabilize the nanoparticles during the creation of the nanocomposite. Differential pulse voltammetry (DPV) test results revealed that the nanocomposite-modified electrode exhibited excellent selectivity and electrochemical characteristics for the detection of UA, with a linear range of 0.1–2000 μM, limit of detection (LOD) of 3.75 μM, limit of quantification (LOQ) of 11.36 μM, and sensitivity of 1.76 μA μM^{-1} cm^{-2}. These results indicated the synergistic effect of the rGO/AgCo nanocomposite in facilitating a higher conductivity and larger surface sensing area for the LIG electrode. Moreover, with such a low concentration level detection capability, the nanocomposite-modified electrode is suitable to be used for the detection of UA in human body fluids, such as sweat, urine, or blood. Thus, in the future, it could potentially realize a UA screening test alternative with excellent selectivity and sensitivity.

Received 28th June 2025
Accepted 2nd October 2025

DOI: 10.1039/d5ra04596g

rsc.li/rsc-advances

1 Introduction

Uric acid (UA) is the main compound resulting from purine metabolism. An abnormal level of UA is often associated with various diseases, such as hyperuricemia, hypouricemia, arthritis inflammation, or even chronic kidney disease.[1–3] This broad clinical relevance underscores the urgent need for sensitive and selective UA detection methods, particularly for early diagnosis and effective disease management. Hence, it is necessary to realize an early screening method, which is not only low-cost but also sensitive and accurate.

In response to this need, electrochemical biosensor technologies have rapidly advanced, driving a paradigm shift in health diagnostics, especially in real-time, point-of-care (POC) systems. Electrochemical biosensors convert biological recognition events into quantifiable electrical signals, such as

[a]*Lab on Chip Laboratory, Biomedical Engineering Department, School of Electrical Engineering and Informatics, Institut Teknologi Bandung, Bandung, 40132, Indonesia. E-mail: isaa@staff.stei.itb.ac.id*

[b]*Research Center for Nanosciences and Nanotechnology, Institut Teknologi Bandung, Bandung, 40132, Indonesia*

[c]*Department of Nanotechnology, Graduate School, Institut Teknologi Bandung, Bandung, 40132, Indonesia*

[d]*Flexens Laboratory, Department of Electrical Engineering, School of Electrical Engineering, Telkom University, Main Campus, Bandung, 40257, Indonesia. E-mail: sukman@telkomuniversity.ac.id*

[e]*Division of Analytical Chemistry, Faculty of Mathematics and Natural Sciences, Institut Teknologi Bandung, Bandung, 40132, Indonesia*

[f]*Division of Inorganic and Physical Chemistry, Faculty of Mathematics and Natural Sciences, Institut Teknologi Bandung, Bandung, 40132, Indonesia*

[g]*National Nanotechnology Center (NANOTEC), NSTDA, 111 Thailand Science Park, Paholyothin Rd., Klong Luang, Pathum Thani 12120, Thailand*

[h]*Department of Materials Science and Engineering, National Taiwan University of Science and Technology, No. 43 Keelung Road, Sec. 4, Da'an District, Taipei 10607, Taiwan (R.O.C.)*

[i]*Research Center for Nanotechnology Systems – National Research and Innovation Agency (BRIN), Puspitek Area, Tangerang Selatan, 15314, Indonesia. E-mail: murn003@brin.go.id*

[j]*Center of Exellence for Biomedical Healthcare Technology, Research Institute for Sustainable Society, Telkom University, Main Campus, Bandung, 40257, Indonesia*

† Both authors contributed equally.

current, voltage, or impedance.[4,5] Compared with conventional laboratory-based assays, electrochemical sensors offer superior performance in terms of their sensitivity, miniaturization, cost-effectiveness, and operational simplicity, making them highly suitable for continuous health monitoring.[6–8]

The performance of an electrochemical biosensor largely depends on the properties of its working electrode (WE), which serves as the signal transduction interface. To this end, various electrode fabrication techniques have been explored. Screen-printing has gained popularity due to its simplicity and scalability. More recently, laser direct writing (LDW) has garnered attention as an alternative method to fabricate laser-induced graphene (LIG), a porous, conductive carbon material produced by laser scribing of carbon-rich substrates like polyimide.[9,10] LIG electrodes offer several advantages, including high electrical conductivity, mechanical flexibility, and tunable porosity, making them ideal candidates for miniaturized electrochemical platforms.[11] Nonetheless, the pristine LIG often exhibits limited electrochemical activity, necessitating surface modification to enhance its biosensing capabilities.

To enhance the electrochemical properties of LIG, the incorporation of nanomaterials has proven to be an effective strategy. Among these, reduced graphene oxide (rGO) has shown potential due to its large surface area, excellent mechanical strength, and improved electron mobility, making it a suitable support for catalytically active nanoparticles.[12–14] In parallel, bimetallic nanoparticles–particularly those combining silver (Ag) and cobalt (Co) have demonstrated superior electrocatalytic properties compared to their monometallic counterparts, due to their synergistic electronic and geometric effects.[15,16] These hybrid structures not only increase the density of active sites, but also facilitate comparably faster electron-transfer kinetics, thereby enhancing both sensitivity and selectivity in electrochemical detection.

Despite the promise of metal nanoparticles, their conventional synthesis methods often involve hazardous chemicals, high temperatures or complex procedures. As a suitable alternative, green synthesis approaches have garnered significant attention. These methods leverage biological systems or natural extracts—such as those from plants, fungi, bacteria, and honey—as reducing and stabilizing agents for producing nanomaterials under mild, non-toxic conditions.[17–19]

Among various natural reagents, honey has attracted attention as a versatile green reductant and capping agent due to its abundant content of polyphenols, sugars, and antioxidants—offering a biocompatible and low-toxicity route for the fabrication of metal-based nanocomposites.[20–22] Honey not only aligns with environmentally friendly principles for synthesis, but also improves nanoparticle dispersibility and biocompatibility—critical factors for biomedical and sensor applications.

Honey contains several components, such as sugars, flavonoids, phenolic compounds, and organic acids. In previous studies, honey showed potential for reducing and stabilizing metallic ions. Monosaccharides, especially fructose and glucose, have been reported as sugars that are reducing agents; these components account for the reducing properties of honey.[23] Additionally, glucose and fructose in honey also demonstrate a reaction with Tollens' reagent,[24] which indicate their capability to reduce Ag^{+} to Ag^{0}. Along with glucose and fructose, other enzymes in honey, such as glucose oxidase, catalase, and peroxidase potentially play a role in the formation of metal oxides. Moreover, phenolic acids have reportedly served as reducing and dispersing agents, while simultaneously refining the stability of nanoparticles.[25]

For UA detection, green-synthesized nanomaterials present a compelling opportunity for enhancing the performance of LIG-based biosensors. Recent studies have demonstrated that LIG electrodes functionalized with metal nanoparticles—such as gold, silver, and copper—enable the sensitive detection of UA in complex biological fluids including sweat, serum, and urine.[1,10,26] For instance, flexible LIG electrodes functionalized with gold nanoparticles enabled the simultaneous detection of UA and dopamine in serum samples.[26] Honey-assisted nanocomposites have shown promise for enhancing the stability and catalytic efficiency of metal-based sensors. Therefore, together, these advances highlight the synergistic potential of integrating green-synthesized nanomaterials with LIG platforms to develop next-generation, eco-friendly biosensors tailored for portable and point-of-care UA monitoring.

In this study, we demonstrated an electrochemical biosensor based on a LIG electrode modified with an rGO/AgCo nanocomposite (LIG/rGO/AgCo electrode) for the sensitive and selective detection of UA. The synthesis of the nanocomposite was carried out using a novel green synthesis method utilizing honey as a mediator. Extensive evaluations of the materials using scanning electron microscopy (SEM), Raman spectroscopy, UV-vis spectrophotometry, and X-ray diffraction (XRD) analysis confirmed the chemical formation of the rGO/AgCo nanocomposite. Moreover, the results of the electrochemical tests showed that the nanocomposite-modified electrode was highly selective toward only UA and yielded a sensitivity of 1.76 $\mu A\ \mu M^{-1}\ cm^{-2}$. These results showcase the suitability of eco-friendly honey as a mediator for producing nanoparticles and the excellent suitability of a surface-modified LIG electrode as an electrochemical biosensor for uric acid detection.

2 Experimental methods

2.1 Chemicals and instruments

Graphite powder, potassium permanganate ($KMnO_4$), hydrogen peroxide (H_2O_2), hydrochloric acid (HCl), cobalt nitrate ($Co(NO_3)_2 \cdot 6H_2O$), silver nitrate ($AgNO_3$), nickel(II) nitrate hexahydrate ($Ni(NO_3)_2$), sulfuric acid (H_2SO_4; 95–97%, sodium nitrate ($NaNO_3$), anhydrous D(+)–glucose ($C_6H_{12}O_6$) powder (95.5–102.0%, uric acid ($C_5H_4N_4O_3$) powder (≥99%, L(+)–ascorbic acid ($C_6H_8O_6$) powder (≥99.7%, and 5% Nafion were procured from Merck (Darmstadt, Germany). The synthetic urine (Sigmatrix urine diluent) solution, which contained calcium chloride ($CaCl_2$), magnesium chloride ($MgCl_2$), potassium chloride (KCl), sodium chloride (NaCl), sodium

phosphate, sodium sulfate (Na_2SO4), urea, and creatinine with sodium azide (NaN_3) as a preservative, was purchased from Sigma-Aldrich (St. Louis, Missouri, United States). Potassium ferricyanide ($K_3[Fe(CN)_6]$) and sodium dihydrogen phosphate ($NaH_2PO_4 \cdot 2H_2O$) at 99% concentration were procured from Loba Chemie (Mumbai, India). Lactic acid (CH_3–CHOH–COOH) at 88–92% concentration was procured from Rofa Laboratorium (Bandung, Indonesia). The phosphate buffer (PB) solution consisting of disodium hydrogen phosphate ($Na_2HPO_4 \cdot 12H_2O$) at 98% was purchased from Pudak Scientific (Bandung, Indonesia). PT Ultra Sakti, Indonesia, provided the natural honey. The LIG electrodes were fabricated by following previously published procedures.[27] The PCB solder mask photoresist ink was locally procured. The silver(II) chloride (Ag/AgCl) paste was purchased from Sun Chemical, United States.

The characterizations of GO, rGO, and rGO/AgCo were carried out using SEM-EDX (FESEM JIB-4610F, EDX Oxford Instruments X-MaxN), HR-TEM (HRTEM JEOL JEM-1400 USA Inc), Raman spectroscopy (Labspec 6-HORIBA iHR320), UV-vis spectrophotometry (Labtron LUS-B11), FT-IR (Prestige 21), and XRD (Smartlab Rigaku). All electrochemical measurements were carried out using a PalmSens4 potentiostat purchased from PalmSens BV.

2.2 *In situ* synthesis of rGO/AgCo

Firstly, GO was synthesized from graphite *via* a modified Hummers' method.[28] The synthesis of rGO/AgCo was then carried out by adding 500 mg of GO to 500 mL distilled water, followed by sonication for 8 × 15 minutes. Twenty grams of natural honey in 50 mL distilled water was then added to the solution and stirred until homogenous. Thereafter, 200 mg of $AgNO_3$ in 50 mL distilled water and $Co(NO_3)_2 \cdot 6H_2O$ were added and the mixture refluxed at 100 °C for 7 hours. The separation of the precipitates was then done by centrifugation, followed by drying in oven at 80 °C for 16 hours. This whole process is illustrated in Fig. 1.

2.3 Preparation of nanocomposite-modified LIG electrode

Firstly, the LIG electrodes were fabricated in a three-electrode configuration comprising the reference electrode (RE), working electrode (WE), and counter electrode (CE). The Ag/AgCl paste was then painted only onto the RE. Ag paste was used as a conductive path and connector by painting it on the connector path of each electrode. After drying the paste, the dielectric layer was painted, covering all the electrodes and isolating the sensing area. The electrodes were then exposed to UV light to cure the dielectric layer. Afterwards, the electrode was modified using the drop-casting method. The rGO/AgCo suspension was firstly prepared by dissolving rGO/AgCo in distilled water in a 10 : 1 ratio, while 5% Nafion for binding was dissolved in ethanol in a 1 : 20 ratio. About 10 μL of the rGO/AgCo suspension was drop-casted only onto the WE, followed by drop-casting of 2.5 μL Nafion (after the rGO/AgCo film dried). These steps are illustrated in Fig. 2.

2.4 Electrochemical characterizations

For characterization using the $K_3[Fe(CN)_6]$ electrolyte, $K_3[Fe(CN)_6]$ with a concentration of 5 mM in 0.1 M PB (pH 7) solution was used in all CV and DPV tests. For the basic CV test, the scan rate was set to 50 mVs^{-1} and the sweep voltage was −0.2 to 0.6 V.

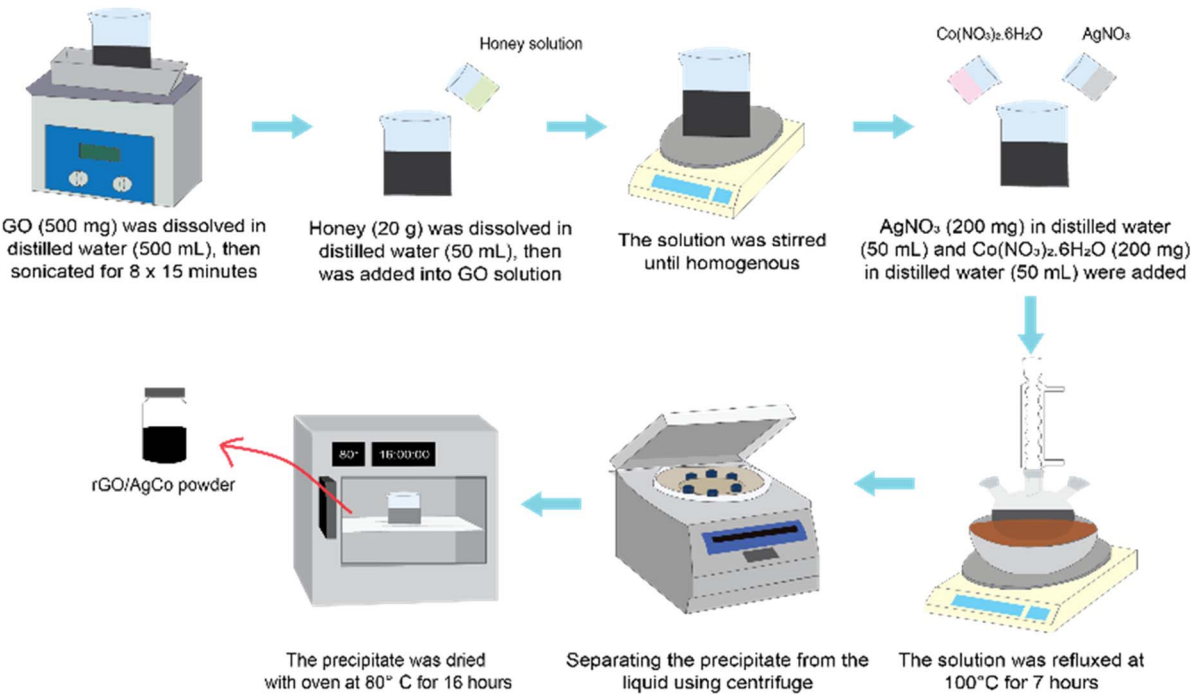

Fig. 1 Preparation of the rGo/AgCo nanocomposite using natural honey as a mediator.

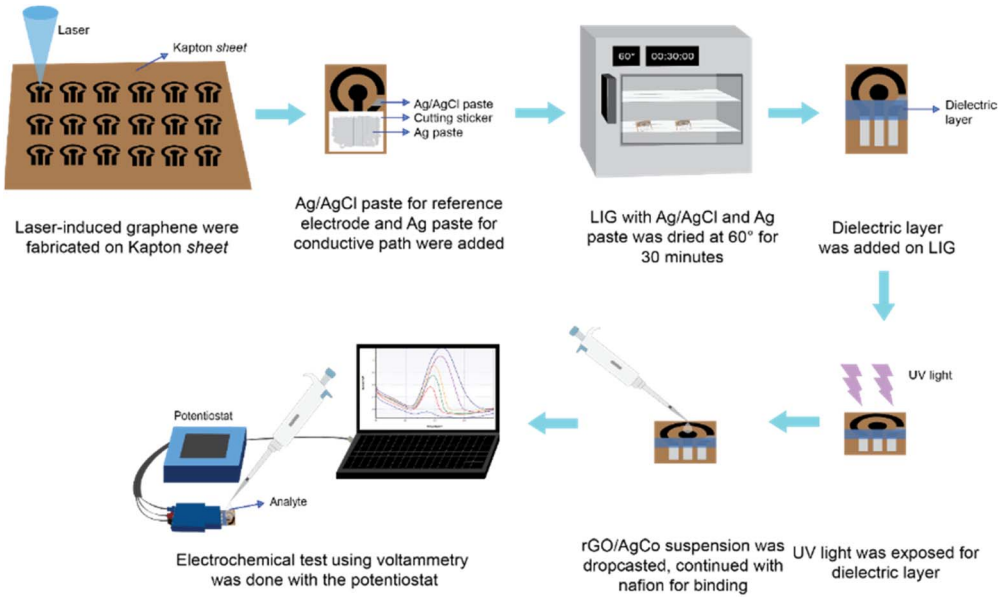

Fig. 2 Preparation of the nanocomposite-modified LIG electrochemical biosensor.

For characterization using UA, UA was dissolved in 0.1 M PB (pH 7) solution for all CV and DPV tests. For all CV and DPV tests, the scan rate was set to 50 mV s^{-1}, while the sweep voltage was −0.2 to 0.6 V. For consecutive and long-term stability measurements, the UA concentration was kept at 1 mM. For long-term stability measurements, the electrode was stored in a refrigerator at a constant temperature of 4 °C. For the selectivity test, the concentration of each target analyte was determined according to its lowest levels in sweat: 2 mM for uric acid (UA), 10 μM for ascorbic acid (AA), 10 μM for glucose, 2.5 mM for ethanol, 5 mM for lactic acid (LA), and 5 mM for urea. Each analyte was then dissolved in 0.1 M PB.

Note that all the electrochemical characterization data were displayed per active surface area of the electrode. In this study, the active surface area of the working electrode was determined by calculating its geometric surface area. Since the working electrode was circle-shaped with a diameter of 0.4 cm, the active surface area of the LIG electrode was 0.1257 cm^2.

3 Results and discussion

3.1 Characterizations of the rGO/AgCo nanocomposite

The results of the SEM-EDX characterizations are shown in Fig. 3. From Fig. 3a, GO showed a sheet-shaped morphology that has wrinkles and folds with irregular edges, indicating deformation due to exfoliation during the conversion of graphite to GO.[29] The EDX results in Fig. S1a show that GO had a chemical composition of 77.4% carbon and 22.6% oxygen. For rGO, the morphology also showed a wrinkled surface (Fig. 3b). This surface morphology indicates that the structure of rGO became curved after reduction, which was caused by the removal of oxygen-containing functional groups in GO. This association was further confirmed by EDX analysis, as shown in Fig. S1b. Based on its chemical composition, rGO contained 83.9% carbon and 16.1% oxygen. There was a 6.5% reduction in the oxygen composition of rGO, which indicates the successful reduction of GO. Furthermore, from Fig. 3c, the silver (AgNPs) and cobalt (CoNPs) nanoparticles appeared in the form of white dots (indicated by the yellow circle) that were distributed on the wrinkled rGO surface. This observation was further confirmed by EDX analysis as shown in Fig. S1c. The chemical composition of the nanoparticles was found to be 74.8% carbon, 14.4% oxygen, 9.6% silver, and 1.1% cobalt.

In addition to the morphological and elemental composition analysis by EDX analysis, TEM characterization was further performed to observe structural details at the nanoscale. The TEM images provided clear insights into the morphological features of the synthesized materials. The GO sample (Fig. S2a) exhibited thin, wrinkled, sheet-like structures, which are a distinctive characteristic of the graphene oxide layers. Upon reduction, the rGO sample (Fig. S2b) showed a more transparent and less defective sheet structure, indicating the partial removal of oxygen-containing groups. For the rGO/AgCo nanocomposite (Fig. S2c and d), the TEM micrographs revealed dark contrast regions, which corresponded to the uniformly distributed AgCo nanoparticles anchored on the rGO sheets. Furthermore, the AgCo nanoparticles were well-dispersed on the nanosheets of rGO without any noticeable aggregation outside the graphene support, which strongly indicated robust interfacial interactions between the rGO layers and the nanostructures. TEM analysis (Fig. S2c) further confirmed that the AgCo nanoparticles possess a relatively narrow particle size distribution in the range of 30–50 nm, with a diameter of approximately 40.3 nm; thereby, validating the effective anchoring and stabilization of AgCo on the rGO support.

Further characterizations were also carried out through Raman spectroscopy, as shown in Fig. 3d. The D band peaks of GO, rGO, and rGO/AgCo were at 1342, 1347, and 1345 cm^{-1},

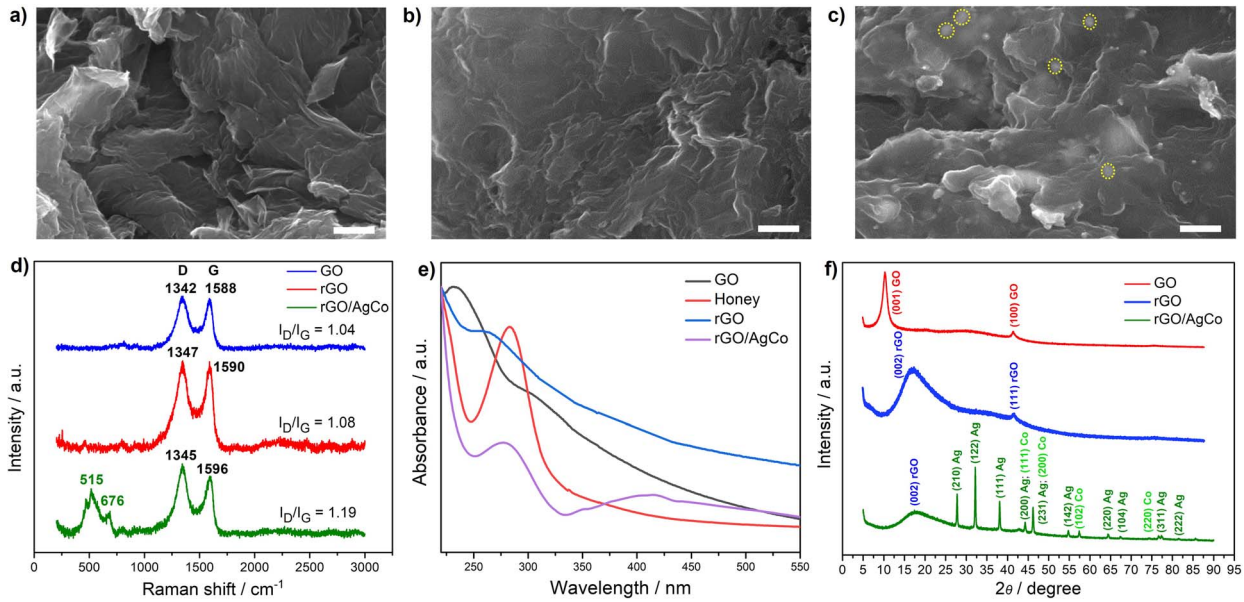

Fig. 3 SEM images of (a) GO, (b) rGO, and (c) the rGO/AgCo nanocomposite (scale bar: 500 nm) along with their corresponding (d) Raman spectra, (e) UV-vis spectra, and (f) XRD patterns.

respectively, while the G band peaks were at 1588, 1590, and 1596 cm^{-1}, respectively. The intensity ratios between the D and G bands (I_D/I_G) for rGO/AgCo, rGO, and GO were 1.19, 1.08, and 1.04, respectively. This ratio increment was due to the AgCo decoration on the rGO sheet, which caused surface-enhanced Raman scattering (SERS).[30] Furthermore, the appearance of distinctive peaks at 515 cm^{-1} and 676 cm^{-1} confirmed the decoration of AgCo on the rGO sheet.[31]

Additionally, the effect of honey as the reducing agent was evaluated by UV-vis measurements. These results are shown in Fig. 3e. For comparative purposes, UV-vis measurements for honey and AgCo were also carried out. From Fig. 3e, GO had a main absorbance peak at 230 nm, which corresponded to the π–π* transition of the C=C bond.[32] Meanwhile, a peak at around 300 nm corresponded to the *n*–π* transition of the C=O bond.[32] The effect of honey as a reducing agent can be clearly seen, especially in the spectra of AgCo and rGO/AgCo, which showed distinctive peaks at 284.5 and 274.5 nm, respectively. Those peaks are typical optical characteristics of honey. Further investigation into the chemical composition and consistency of honey as a reducing agent is provided in Note S1.

Apart from the influence of honey, the shift in the peak of rGO indicated a conjugation of the GO sheets due to the reduction of GO to rGO.[33] Moreover, from the rGO/AgCo spectra, the peaks at 274.5 nm, 404.5 nm, and 510 nm indicated the successful reduction of GO with honey as a reducing agent and the presence of AgCo on the surface of rGO.[34] In addition, a weak shoulder around 510 nm was observed, which can be ascribed to the charge-transfer transitions of the Co species ($O^{2-} \rightarrow Co^{2+}/Co^{3+}$), consistent with previous reports of Co_3O_4 nanoparticles.[35,36]

Additionally, the XRD pattern was also analyzed for evaluating the crystal structure of the rGO/AgCo nanocomposite (Fig. 3f). The peaks can be divided into three parts, namely those of rGO, AgNPs, and CoNPs. The peak at 17.7° indicated the (002) plane belonging to rGO. By referring to JCPDS 04-0783 database,[37] AgNP showed diffraction peaks at 27.8°, 32.2°, 38.1°, 44.3°, 46.3°, 54.8°, 64.5°, 67.5°, 77.5°, and 81.6°, which respectively denoted the (210), (122), (111), (200), (231), (142), (229), (104), (311), and (222) planes. By referring to the JCPDS 15-0806 database,[38] CoNPs displayed diffraction peaks at 44.3°, 46.3°, 57.5°, and 76.8°, which respectively indicated the (111), (200), (102), and (220) planes. Therefore, these peaks indicated that the AgNPs and CoNPs contained in the nanocomposite had a face-centered cubic (fcc) crystal structure.[39]

3.2 Electrochemical biosensing characterization using $K_3[Fe(CN)_6]$

3.2.1 Scan rate variations. Variations in the scan rate were tested to determine the reaction mechanism that occurred on the surface of the electrodes (bare LIG and LIG/rGO/AgCo). The results of the bare LIG electrode, depicted in Fig. 4a and b, show a reversible reaction, which resulted in an increase in the current density as the scan rate increased. This result was not much different for the LIG/rGO/AgCo electrode (Fig. 4c and d); it also showed a reversible reaction with an increasing current density as the scan rate increased. The calibration curves of the peak redox current density (j_p) against the square root of the scan rate ($v^{1/2}$) are shown in Fig. 4b and d. The calibration curves of the bare LIG and LIG/rGO/AgCo electrodes showed a linear relationship between j_p and $v^{1/2}$. In addition, the LIG/rGO/AgCo electrode showed a better linearity than that of the bare electrode, showcasing better electrocatalytic activity for the redox reaction.

Additionally, both the bare LIG and LIG/rGO/AgCo electrodes also displayed a reversible reaction, resulting in a monotonous increase in the current density with respect to the square root of the scan rate. This corresponds to the following Randles–Ševčik equation:

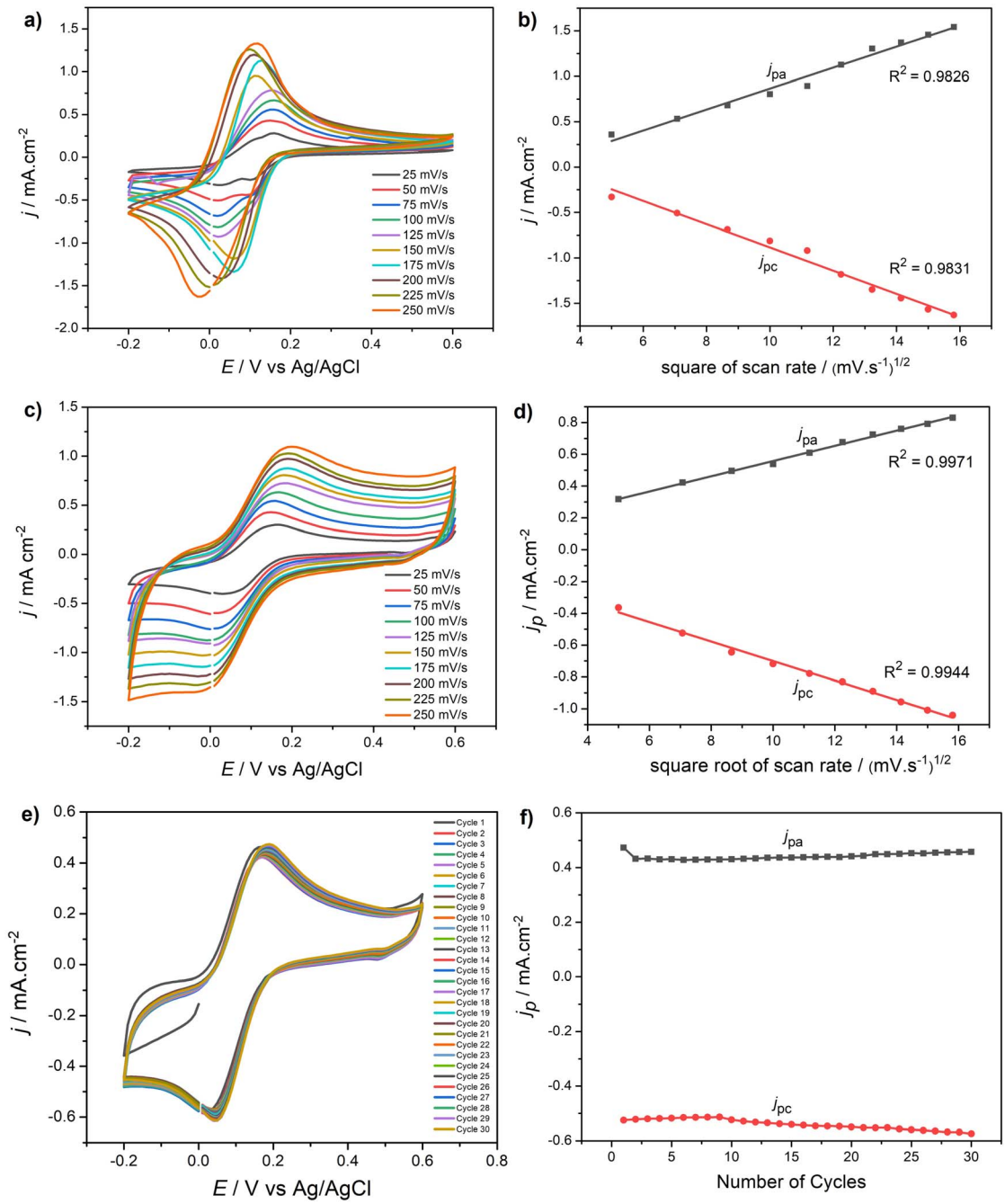

Fig. 4 Basic electrochemical biosensing characterization using the redox-active KFeCN electrolyte. (a) Scan rate variation test on the bare LIG electrode along with the corresponding (b) calibration curve. (c) Scan rate variation test on the LIG/rGO/AgCo electrode along with the corresponding (d) calibration curve. (e) 30-cycle of consecutive CV test on the LIG/rGO/AgCo electrode along with the corresponding (f) calibration curve.

$$I_p = 2.69 \times 10^5 A D^{1/2} n^{3/2} v^{1/2} C$$

where I_p denotes the peak current value per electroactive area (A), also known as current density (j_p), which is proportional to the square root of the scan rate ($v^{1/2}$), diffusion coefficient value ($D^{1/2}$), and the number of electrons in the redox reaction ($n^{3/2}$) at a given concentration value (C). This expression indicates that the voltammetric response of the electrode in the $K_3[Fe(CN)_6]$ electrolyte was based on a diffusion-controlled mechanism.[40]

3.2.2 Consecutive measurements of stability. Consecutive measurements were carried out using CV for 30 cycles at a scan rate of 50 mV s^{-1} (Fig. 4e), and the corresponding calibration curves for the anodic and cathodic peak current densities are shown in Fig. 4f. It can be observed that there was an increasing tendency in the anodic peaks and a decreasing tendency in the cathodic peaks. To provide a quantitative evaluation of these observations, the relative error was calculated for each peak using the following equation:[41]

$$\text{Relative error} = \left|\frac{\text{Peak current density of cycle } x - \text{Reference}}{\text{Reference}}\right| \times 100\%$$

The reference value used was the peak current density of the first cycle. The results of the relative error calculation were then averaged for all cycles.

The anodic peak current density ranged from 0.42 to 0.47 mA cm^{-2}, while the cathodic peak current density ranged from 0.51 to 0.57 mA cm^{-2}. The average relative errors for the anodic and cathodic peak current densities were 6.7% and 3.7%, respectively. Thus, it can be concluded that the electrochemical characteristics of the LIG/rGO/AgCo electrode were stable for consecutive measurements.

3.3 Detection performance for UA

3.3.1 Comparison of bare LIG with modified LIG electrodes. Initially, the electrodes were characterized using a $K_3[Fe(CN)_6]$ electrolyte. The results, depicted in Fig. 5a, showed that all the electrodes were able to reversibly perform the redox reaction:

$$[Fe(CN)_6]^{3-} + e^- \rightleftharpoons [Fe(CN)_6]^{4-}$$

The LIG/rGO/AgCo electrode showed a slightly better performance in terms of its anodic and cathodic current density than other electrodes. The increase in current density indicated that the electroactive area increased due to surface modification. This increase was associated with the rGO sheet, which had a large surface area, as well as the AgCo bimetal, which provided many active sites that increased the catalytic activity.[42]

In detail, the anodic current density (j_{pa}) increased by 11.7% and the cathodic current density (j_{pc}) increased by 17.9% for the LIG/rGO electrode when compared with the bare LIG. Moreover, when the bare LIG is compared with the LIG/rGO/AgCo electrode, j_{pa} and j_{pc} increased by 13.3% and 18.8%, respectively. These results indicate that rGO had already improved the catalytic activity of the electrode and further improvement was achieved by the rGO/AgCo electrode due to the synergistic combination of the large surface area and conductivity of the nanocomposite.[43]

Afterwards, the detection of UA analyte was evaluated by CV test. Firstly, the CV tests were conducted on the bare LIG, LIG/rGO, and LIG/rGO/AgCo electrodes. The CV curves of the UA detection result (Fig. 5b) showed a quasi-reversible electrochemical reaction in all three types of electrodes, which was indicated by a high oxidation peak with a very low reduction peak.[44] The oxidation reaction of UA to allantoin, which indicates a quasi-reversible reaction with the involvement of two-electron transfer can be expressed as follows.[45]

$$C_5H_4N_4O_3 \xrightarrow{2H^+ + 2e^-} C_4H_6N_4O_3$$

Furthermore, based on the results in Fig. 5b, the oxidation of UA on the LIG/rGO/AgCo electrode exhibited the highest anodic current density. The increase in current density indicates that the electroactive area increased due to modification with the nanocomposite, resulting in rGO having a larger active surface area and AgCo providing more active reaction sites.[42] In detail, the average anodic peak current density (j_{pa}) for the bare LIG, LIG/rGO, and LIG/rGO/AgCo electrodes were 0.143, 0.308, and 0.531 mA cm^{-2}, respectively. This means that there was an obvious increase in j_{pa} by 115% for the LIG/rGO electrode and 271% for the LIG/rGO/AgCo electrode when compared with the bare LIG. Hence, these results confirm that surface modification using the rGO/AgCo nanocomposite can facilitate a significant improvement due to the combination of the large surface area with the synergistic conductivity.[43] Further insight regarding this phenomenon was also elaborated through electrochemical impedance (charge-transfer resistance) analysis provided in Note S2.

3.3.2 Scan rate variations. To understand the reaction kinetics that occurred on the surface of the modified LIG electrode, the scan rate was varied. In this test, the scan rate was varied from 25, 50, 75, 100, 125, 150, 175, 200, and to 225 mV s^{-1}. Based on Fig. 5c, the intensity of both the oxidation and reduction currents increased proportionally as the scan rate increased. This result demonstrates that the conductivity of the electrode's surface was gradually enhanced as the electron-charge transfer rate rose.[46] This result also indicates that UA oxidation is a quasi-reversible reaction.[44]

Additionally, a calibration curve of the peak oxidation current density (j_p) against the square root of the scan rate ($v^{1/2}$) was plotted. From the calibration curve in Fig. 5d, a linear response with increasing scan rate was observed. This result indicates that the reaction kinetics were due to a diffusion mechanism, in accordance with the Randles–Ševčik equation.[47]

3.3.3 LIG/rGO/AgCo electrode for UA detection. The performance of the LIG/rGO/AgCo electrode for detecting UA was evaluated using DPV, in which the UA concentration (0.1, 0.5, 1, 5, 10, 50, 100, 250, 500, 750, 1000, 1500, and 2000 μM) was varied. As shown in Fig. 5e, the peak current density increased as the UA concentration increased.

Additionally, Fig. 5e also shows that the peak potential shifted towards more positive values as the analyte concentration increased. This behaviour most likely originated from the uncompensated solution resistance, which is referred to as an iR drop. As the analyte concentration increased, the oxidation current also increased and caused a greater voltage drop across the solution resistance.[48] This voltage loss caused the measured oxidation peak potential to appear more positive since a higher potential was applied to overcome the resistance. Nonetheless, the distinctive increase of the oxidation peak was clearly observable upon increasing the UA concentration; this increase was used as the main performance indicator for our electrode. The corresponding calibration curve of the LIG/rGO/AgCo electrode is depicted in Fig. 5f. From the curve, the limit of detection (LOD) and the limit of quantification (LOQ) were determined using the equations below, where σ denotes the standard deviation of the peak current density of the blank response (0 mM UA in PB) and S is the slope of the calibration curve or its sensitivity.

$$\text{LOD} = 3.3 \times \sigma/S$$

$$\text{LOQ} = 10 \times \sigma/S$$

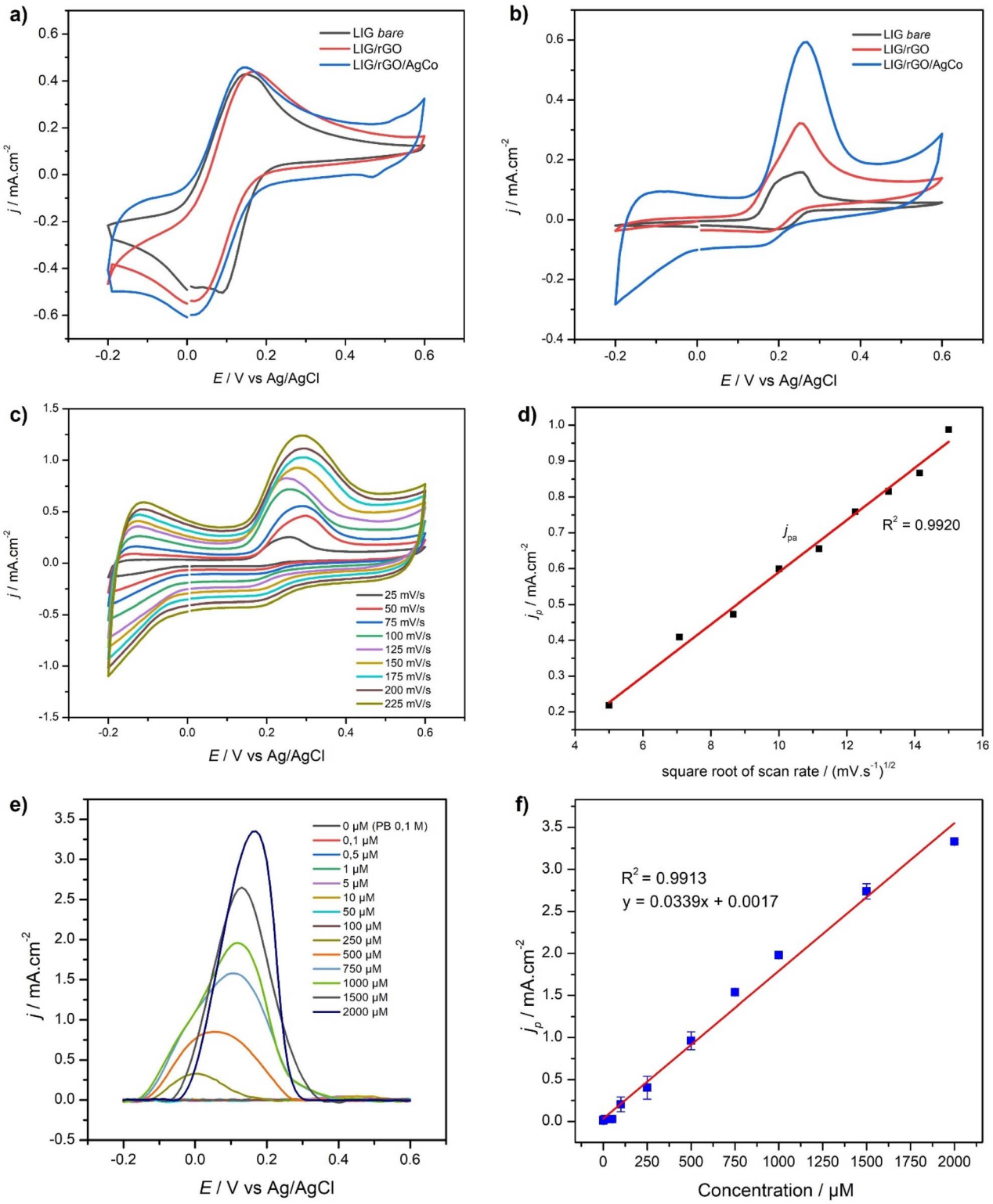

Fig. 5 CV test results for the bare LIG, LIG/rGO, and LIG/rGO/AgCo electrodes using (a) $K_3[Fe(CN)_6]$ electrolyte and (b) UA target analyte. (c) Scan rate variation test on the LIG/rGO/AgCo electrode for detecting the target analyte UA along with the corresponding (d) calibration curve. (e) DPV tests on the LIG/rGO/AgCo electrode for detecting the target analyte UA, along with the corresponding (f) calibration curve.

From these two equations and the calibration curve, the calculated LOD was 3.75 µM and the LOQ was 11.36 µM. Additionally, the linear range was 0.1–2000 µM.

A comparison with other studies that used electrochemical biosensors for the detection of UA is provided in Table 1. From the comparison, the detection range of the LIG/rGO/AgCo

Table 1 Performance comparison of the electrochemical biosensor electrodes for UA detection

Electrode	Method	Linear range (μM)	LOD (μM)	LOQ (μM)	Sensitivity	Reference
GCE/rGO/AgNP[a]	DPV	10–130	1	3.03	0.084 μA μM^{-1}	12
GCE/UOx/Fc/Cu_2O[b]	CV	0.1–1000	0.059	0.181	1.900 μA mM^{-1} cm^{-2}	50
GCE/Fe/CuO[c]	CV	50–4000	10	30.3	2.719 μA mM^{-1}	47
CPE/Fe_3O_4/SiO_2/MWCNT[d]	SWV	0.6–100	0.13	0.394	0.003 μA μM^{-1}	51
SPCE/Nafion[e]	DPV	62.5–5000	20.8	63.03	9.366 μA μM^{-1}	52
SPE/AuNP[f]	CA	20–200	11.91	36.09	0.22 μA μM^{-1}	53
LIG/PtNP[g]	DPV	1–63	0.22	0.67	8.289 μA μM^{-1} cm^{-2}	40
LIG/PBSE/PtNP[h]	DPV	5–480	0.018	0.055	0.157 μA mM^{-1} cm^{-2}	54
LIG/Chitosan/AuNP[i]	DPV	30–100	0.33	1.10	0.48 μA μM^{-1}	55
LIG/rGO/AgCo	**DPV**	**0.1–2000**	**3.75**	**11.36**	**1.76 μA $\mu M^{-1}cm^{-2}$**	**This work**

electrode in this study was wider than the other biosensors, and it had comparable LOD and LOQ values. The wide linear range of LIG/rGO/AgCo indicated a high interval of the lowest and the highest target analyte concentration it can detect in a sample.

3.3.4 Consecutive measurements of stability. Consecutive measurements were repeated for 80 cycles. The result of these measurements is shown in Fig. 6a, while the peak current density calibration curve is shown in Fig. 6b. The total measurement showed a rather unstable output current density. The decrease and instability of this response could be caused by undesired damage to the surface of the working electrode due to repeated use of the same target analyte.[49] However, the response was still quite stable for up to 30 cycles with an average relative error of 6.9%. When compared to the stability test conducted in

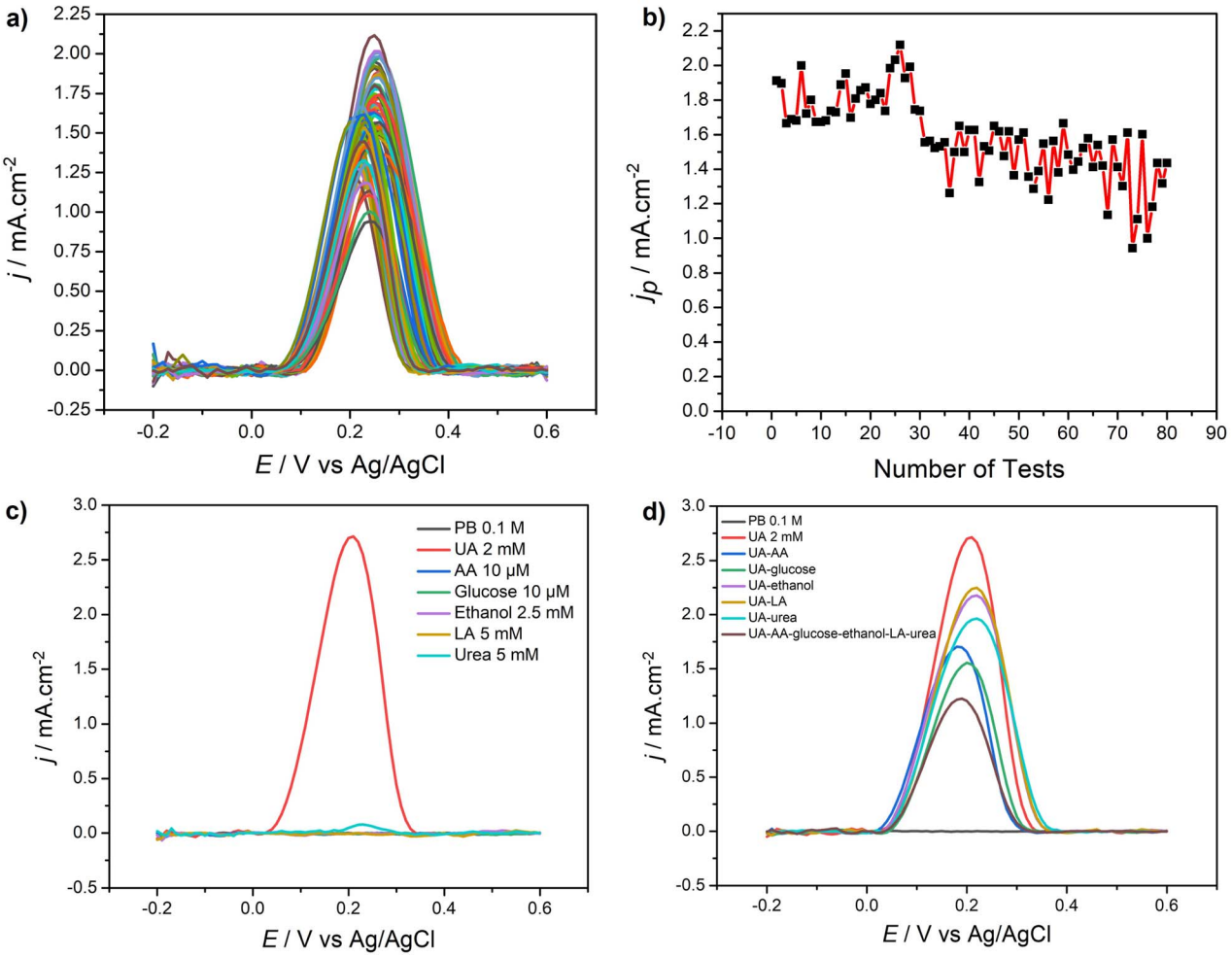

Fig. 6 (a) Consecutive 80-cycle DPV test on the LIG/rGO/AgCo electrode along with (b) the corresponding calibration curve. Selectivity test of the LIG/rGO/AgCO electrode for the detection of (c) various target analytes and (d) interfering compounds. (Note: PB = phosphate buffer, AA = ascorbic acid, LA = lactic acid).

a prior study,[44] the relative error of the response was 2.3% for 10 cycles. From this comparison, the stability of the LIG/rGO/AgCo electrode as evaluated from consecutive measurements was stable enough, considering the relatively large number of repeated measurements.

3.3.5 Long-term measurements of stability. In addition to being tested for stability in consecutive measurements, the LIG/rGO/AgCo electrode was also tested for its long-term use. In this test, the LIG/rGO/AgCo electrode was stored for 2 months, and its electrochemical performance was measured periodically. Based on the measurements shown in Fig. S3a and S3b, the peak current density decreased over time.

This decrease in performance was likely due to the testing of LIG/rGO/AgCo in the first week using DPV, which was performed several times with 1 mM UA to obtain the best peak current density value. In addition, the measurements performed over 2 weeks were enough to result in a decreased value; this phenomenon is known as biosensor ageing, which is a decrease in the electrochemical response at a certain concentration of analytes measured over a certain period of time.[49] Therefore, these results suggest that the repeated use of the LIG/rGO/AgCo electrode would produce the best result when measurement is carried out only within the first week.

3.3.6 Influence of electrolyte pH on uric acid detection. Since UA is a weak diprotic acid, its electrochemical behaviour strongly depends on the protonation state of its functional groups. The electrolyte pH is expected to play a crucial role during oxidation. To gain deeper insights into this effect, we evaluated the current of the LIG/rGO/AgCo electrode in 1 mM UA using phosphate-buffered solutions at different pH values (6.0, 7.0, and 8.0). As shown in Fig. S4, the peak current density increased from pH 6.0 to pH 7.0, reaching a maximum response at pH 7.0. However, when the pH further increased to 8.0, the current decreased. This trend indicated that the catalytic activity of the modified electrode for uric acid oxidation was pH-dependent.

The enhanced current response from pH 6.0 to 7.0 was attributed to the increased availability of the deprotonated uric acid species, which facilitated the electron-transfer process.[56] Beyond pH 7.0, the decreased current response most probably resulted from the instability of uric acid and the reduced catalytic efficiency of uricase under alkaline conditions.[57] Therefore, pH 7.0 was considered the optimal condition for UA detection in this system. This is also consistent with the previously reported optimum enzymatic activity of uricase, which was at a near-neutral pH.[58]

3.3.7 Selectivity. Testing for selectivity was conducted using DPV and the results are shown in Fig. 6c. Based on Fig. 6c, it is obvious that the LIG/rGO/AgCo electrode was highly selective to UA, slightly selective to urea, and did not give any response to other analytes. Another test for selectivity was conducted by placing the electrode in a solution containing UA and other interfering compounds, which were UA–AA, UA–LA, UA–ethanol, UA–glucose, UA–urea, and UA–AA–LA–ethanol–glucose–urea. Based on the results shown in Fig. 6d, the response curve of UA had the highest peak current density, followed by those of UA–LA, UA–ethanol, UA–urea, UA–AA, UA–glucose, and UA–AA–LA–ethanol–glucose–urea. From these two results, it is clear that the peaks that appeared when the solutions were tested simultaneously (UA with interfering compounds) were indeed only affected by the existence of UA. In other words, the interfering compounds only changed the height of the peak response, while the LIG/rGO/AgCo electrode still showed selectivity for UA.

3.3.8 Performance evaluation in synthetic urine. The performance of LIG/rGO/AgCo in complex matrices was assessed using synthetic urine spiked with uric acid as shown in Fig. S5. The system exhibited an R^2 value of 0.9351, a LOD of 34.31 μM, and a LOQ of 103.98 μM. In comparison, measurements in a pure uric acid solution displayed superior performance, highlighting a notable decrease in sensitivity and precision in the synthetic urine matrix.

This reduction can be attributed to the complex composition of synthetic urine, which likely introduced other foreign interfering species, which affected electron transfer at the sensor's interface.

Despite this observation, a reasonably linear correlation between the response and uric acid concentration was maintained, and the LOD and LOQ remained within a biologically relevant range. These findings underscore that while the system was capable of selectively detecting uric acid in complex, biologically relevant matrices, the performance was considerably impacted. This result suggests that further optimization or matrix-specific calibration might be necessary for accurate quantification in real biological test samples.

4 Conclusions

This study demonstrated a novel green synthesis of an rGO/AgCo nanocomposite that was achieved by utilizing honey as a reducing agent and applying it as a surface modifier on a LIG electrode for UA detection. The surface morphology of the electrode exhibited wrinkled sheets associated with rGO and white dots corresponding to the AgCo bimetallic nanoparticles. In addition, the Ag and Co nanoparticles were found to possess a face-centered cubic (fcc) crystalline structure. These combined morphological and crystalline characteristics contributed to an enlarged surface area for sensing and an abundance of active sites for UA detection. Thus, these characteristics account for the higher output current response of the LIG/rGO/AgCo electrode for UA detection compared to the bare LIG or LIG/rGO electrodes, as demonstrated by the CV results. This response increased by 271% relative to the bare LIG. Furthermore, the LIG/rGO/AgCo electrode exhibited a wide linear range of 0.1–2000 μM with a LOD of 3.75 μM, LOQ of 11.36 μM, and sensitivity of 1.76 μA μM^{-1} cm^{-2}. It also demonstrated stable consecutive measurements for up to 30 cycles. Moreover, the LIG/rGO/AgCo electrode showcased an excellent selectivity toward UA, even in the presence of various interfering analytes, including ascorbic acid, lactic acid, ethanol, glucose, and urea. These results highlight the potential of the nanocomposite-modified LIG electrode as a sensitive and highly selective electrochemical biosensor for UA detection.

Author contributions

I. A.: conceptualization, funding acquisition, resources, methodology, supervision, writing – review & editing. A. R. A.: data curation, formal analysis, writing – original draft. U. & S. H.: formal analysis, validation, visualization, writing – review & editing. N. H., V. S., M. A. Z.: funding acquisition, investigation. A. K.: resources. C. Y. C.: funding acquisition. M. H.: methodology, validation, supervision, writing – review & editing.

Conflicts of interest

There are no conflicts to declare.

Data availability

The data supporting this article have been included as part of the supplementary information (SI). Supplementary information: EDX analysis and TEM images of the nanocomposite materials, long-term electrocatalytic performance of the LIG/rGO/AgCo electrode for UA detection, DPV measurements of the LIG/rGO/AgCo electrode under different electrolyte pH values, UA detection performance of the LIG/rGO/AgCo electrode in synthetic urine solution, FTIR analysis of honey samples, and electrochemical impedance analysis of the modified and unmodified electrodes. See DOI: **https://doi.org/10.1039/d5ra04596g**.

Acknowledgements

This research received financial support from the Directorate of Research and Innovation (DRI), Institut Teknologi Bandung, through ITB-NTUST Joint Research Program [contract no. 9522/IT1.B07.1/TA.00/2023]. Additional support was provided by the Hibah DTTP 2025 [contract no. 2797/IT1.B07.5/TA.00/2025], managed by the Directorate of Research and Innovation (DRI), Institut Teknologi Bandung. The authors appreciate and acknowledge the technical support provided by the Advanced Characterization Laboratories Serpong, a facility supported by the National Research and Innovation Agency through E-Layanan Sains, Badan Riset dan Inovasi Nasional.

References

1 B. Kulyk, S. O. Pereira, A. J. S. Fernandes, E. Fortunato, F. M. Costa and N. F. Santos, *Carbon N. Y.*, 2022, **197**, 253–263.
2 Y. Han, M. Yao, H. Zhao, X. Han, H. Di, T. Xie, J. Wu, Y. Wang, Y. Zhang and X. Zeng, *J. Am. Heart Assoc.*, 2025, **14**, e038723.
3 Y. Liu, Z. Li, Y. Xu, H. Mao and N. Huang, *Kidney Dis.*, 2025, **11**, 112–127.
4 D. Grieshaber, R. MacKenzie, J. Vörös and E. Reimhult, *Sensors*, 2008, **8**, 1400–1458.
5 E. P. Randviir and C. E. Banks, *Anal. Methods*, 2022, **14**, 4602–4624.
6 F. Ceccardi, F. Mariani, F. Decataldo, V. Vurro, M. Tessarolo, I. Gualandi, B. Fraboni and E. Scavetta, *Electrochim. Acta*, 2025, **519**, 145834.
7 S. Thirumalairajan, K. Girija, V. R. Mastelaro, V. Ganesh and N. Ponpandian, *RSC Adv.*, 2014, **4**, 25957–25962.
8 I. Anshori, I. F. Ramadhan, E. Ariasena, R. Siburian, J. Affi, M. Handayani, H. Yunkins, T. Kuji, T. L. E. R. Mengko and S. Harimurti, *IEEE Access*, 2022, **10**, 112578–112593.
9 F. M. Vivaldi, A. Dallinger, A. Bonini, N. Poma, L. Sembranti, D. Biagini, P. Salvo, F. Greco and F. Di Francesco, *ACS Appl. Mater. Interfaces*, 2021, **13**, 30245–30260.
10 S. Choudhury, S. Zafar, D. Deepak, A. Panghal, B. Lochab and S. S. Roy, *J. Mater. Chem. B*, 2024, **13**, 274–287.
11 Z. Wan, N. T. Nguyen, Y. Gao and Q. Li, *Sustainable Mater. Technol.*, 2020, **25**, e00205.
12 S. P. Nayak, S. S. Ramamurthy and J. K. Kiran Kumar, *Mater. Chem. Phys.*, 2020, **252**, 123302.
13 S. Tamang, S. Rai, R. Bhujel, N. K. Bhattacharyya, B. P. Swain and J. Biswas, *J. Alloys Compd.*, 2023, **947**, 169588.
14 P. Manivel, M. Dhakshnamoorthy, A. Balamurugan, N. Ponpandian, D. Mangalaraj and C. Viswanathan, *RSC Adv.*, 2013, **3**, 14428–14437.
15 M. Hafeez, R. Shaheen, B. Akram, Z. Ul-Abdin, S. Haq, S. Mahsud, S. Ali and R. T. Khan, *Mater. Res. Express*, 2020, **7**, 025019.
16 E. S. Aazam and Z. Zaheer, *Arabian J. Chem.*, 2022, **15**, 103795.
17 N. Vidyasagar, R. R. Patel, S. K. Singh and M. Singh, *Mater. Adv.*, 2023, **4**, 1831–1849.
18 S. A. M. Khalifa, A. A. Shetaia, N. Eid, A. A. Abd El-Wahed, T. Z. Abolibda, A. El Omri, Q. Yu, M. A. Shenashen, H. Hussain, M. F. Salem, Z. Guo, A. M. Alanazi and H. R. El-Seedi, *Bioengineering*, 2024, **11**, 829.
19 M. Mylarappa, S. Chandruvasan, K. S. Harisha, R. Sandhya, K. N. Shravana Kumara, S. G. Prasanna Kumar and H. Madival, *Green Technol. Sustainability*, 2024, **2**, 100085.
20 D. Philip, *Spectrochim. Acta, Part A*, 2010, **75**, 1078–1081.
21 E. R. Balasooriya, C. D. Jayasinghe, U. A. Jayawardena, R. W. D. Ruwanthika, R. M. De Silva and P. V. Udagama, *J. Nanomater.*, 2017, **2017**, 5919836.
22 S. G. B. de Souza, K. J. S. Silva, M. M. R. Azevedo, A. K. O. Lima, H. de Campos Braga, D. B. Tada, K. Gul, S. Malik, G. Nakazato and P. S. Taube, *Appl. Nanosci.*, 2023, **14**(1), 191–201.
23 G. Bonsignore, M. Patrone, S. Martinotti and E. Ranzato, *J. Funct. Biomater.*, 2021, **12**, 72.
24 S. Durmazel, A. Üzer, B. Erbil, B. Sayln and R. Apak, *ACS Omega*, 2019, **4**, 7596–7604.
25 N. Bahari, N. Hashim, K. Abdan, A. Md Akim, B. Maringgal and L. Al-Shdifat, *Nanomaterials*, 2023, **13**, 1244.
26 A. Rabti, S. Baachaoui, M. Zouari and N. Raouafi, *J. Pharmaceut. Biomed. Anal.*, 2025, **5**, 100069.
27 S. Inlumphan, W. Wongwiriyapan, N. Khemasiri, P. Rattanawarinchai, P. Leepheng, P. Luengrojanakul, T. Wuttikhun, M. Obata, M. Fujishige, K. Takeuchi, M. P. Reilly, T. Uwanno, M. Horprathum, S. Porntheeraphat, K. Sitthisuwannakul,

S. Phanthanawiboon and A. Klamchuen, *Sens. Acutators Rep.*, 2025, **9**, 100276.
28 H. Yu, B. Zhang, C. Bulin, R. Li and R. Xing, *Sci. Rep.*, 2016, **6**, 1–7.
29 G. Sriram, M. Arunpandian, K. Dhanabalan, V. R. Sarojamma, S. David, M. D. Kurkuri and T. H. Oh, *Inorganics*, 2024, **12**, 145.
30 S. Gurunathan, J. H. Park, Y.-J. Choi, J. W. Han and J.-H. Kim, *Curr. Nanosci.*, 2016, **12**, 762–773.
31 R. Bhujel, S. Rai, Z. Mustafa, G. Sarkar, U. Deka, J. Biswas and B. P. Swain, *AIP Conf. Proc.*, 2020, **2273**(1), 040002.
32 M. Handayani, B. I. Suwaji, G. Ihsantia Ning Asih, T. Kusumaningsih, Y. Kusumastuti, R. Rochmadi and I. Anshori, *Nanocomposites*, 2022, **8**, 74–80.
33 T. Wu, S. Liu, Y. Luo, W. Lu, L. Wang and X. Sun, *Nanoscale*, 2011, **3**, 2142–2144.
34 A. Ashok, A. Kumar and F. Tarlochan, *Nanomaterials*, 2018, **8**, 604.
35 L. A. Kolahalam, K. R. S. Prasad, P. M. Krishna and N. Supraja, *Results Chem.*, 2024, **7**, 101367.
36 S. A. Balogun, T. O. Abolarinwa, F. A. Adesanya, C. N. Ateba and O. E. Fayemi, *J. Anal. Sci. Technol.*, 2024, **15**, 1–14.
37 Y. Meng, *Nanomaterials*, 2015, **5**, 1124–1135.
38 I. Ali, Y. Pan, Y. Lin, Y. Jamil, J. Hu, Z. Gan, J. Chen and Z. Shen, *Appl. Phys. A:Mater. Sci. Process.*, 2021, **127**, 1–10.
39 I. Roy, D. Rana, G. Sarkar, A. Bhattacharyya, N. R. Saha, S. Mondal, S. Pattanayak, S. Chattopadhyay and D. Chattopadhyay, *RSC Adv.*, 2015, **5**, 25357–25364.
40 P. Nayak, N. Kurra, C. Xia and H. N. Alshareef, *Adv. Electron. Mater.*, 2016, **2**, 1600185.
41 J. de Fátima Giarola, V. Mano and A. C. Pereira, *Electroanalysis*, 2018, **30**, 119–127.
42 L. Ai, X. Liu and J. Jiang, *J. Alloys Compd.*, 2015, **625**, 164–170.
43 S. Nasraoui, A. Al-Hamry, A. Anurag, P. R. Teixeira, S. Ameur, L. G. Paterno, M. Ben Ali and O. Kanoun, *16th International Multi-Conference on Systems, Signals and Devices, SSD 2019*, 2019, pp. 615–620.
44 M. Tefera, M. Tessema, S. Admassie and W. Wubet, *Heliyon*, 2021, **7**, e07575.
45 Y. Wen, J. Chang, L. Xu, X. Liao, L. Bai, Y. Lan and M. Li, *J. Electroanal. Chem.*, 2017, **805**, 159–170.
46 S. Priyatharshni, A. Tamilselvan, C. Viswanathan and N. Ponpandian, *J. Electrochem. Soc.*, 2017, **164**, B152.
47 B. Waryani, A. Tahira, S. Ameen, M. Willande, A. R. Abbasi and Z. H. Ibupoto, *J. Electron. Mater.*, 2020, **49**, 6123–6129.
48 Y. Liu, K. J. Aoki and J. Chen, *Electrochem*, 2023, **4**, 460–472.
49 P. Panjan, V. Virtanen and A. M. Sesay, *Talanta*, 2017, **170**, 331–336.
50 Q. Yan, N. Zhi, L. Yang, G. Xu, Q. Feng, Q. Zhang and S. Sun, *Sci. Rep.*, 2020, **10**, 1–10.
51 M. Arvand and M. Hassannezhad, *Mater. Sci. Eng. C*, 2014, **36**, 160–167.
52 Z. Xu, M. qi Zhang, H. qun Zou, J. shan Liu, D. zhi Wang, J. Wang and L. ding Wang, *J. Electroanal. Chem.*, 2019, **841**, 129–134.
53 J. Piedras, R. B. Dominguez and J. M. Gutiérrez, *Chemosensors*, 2021, **9**, 73.
54 M. Faruk Hossain and G. Slaughter, *Bioelectrochemistry*, 2021, **141**, 107870.
55 K. Samoson, A. Soleh, K. Saisahas, K. Promsuwan, J. Saichanapan, P. Kanatharana, P. Thavarungkul, K. H. Chang, A. F. Lim Abdullah, K. Tayayuth and W. Limbut, *Talanta*, 2022, **243**, 123319.
56 B. Kanthappa, J. G. Manjunatha, S. A. Aldossari and C. Raril, *Sci. Rep.*, 2025, **15**, 1–17.
57 Q. Yan, N. Zhi, L. Yang, G. Xu, Q. Feng, Q. Zhang and S. Sun, *Sci. Rep.*, 2020, **10**, 1–10.
58 B. Han, M. Pan, X. Liu, J. Liu, T. Cui and Q. Chen, *Materials*, 2019, **12**, 214.